Journal of Applied Physics

RESEARCH ARTICLE | SEPTEMBER 17 2024

An electro-thermal finite element method (FEM) model for local hotspot kinetics in Cu(In, Ga)Se_2 thin-film solar modules

Suheir Nofal ; Timon S. Vaas ; Uwe Rau ; Bart E. Pieters

J. Appl. Phys. 136, 115102 (2024)
https://doi.org/10.1063/5.0222051

Articles You May Be Interested In

Correlation-based study of FEA and IR thermography to reveal the 2DEG temperature of a multi-fingered high-power GaN HEMT

J. Appl. Phys. (February 2022)

On the origin and evolution of hotspots in multipatterning processes

J. Vac. Sci. Technol. B (June 2023)

Machine learning-assisted thermoelectric cooling for on-demand multi-hotspot thermal management

J. Appl. Phys. (June 2024)

29 June 2026 17:12:38

AIP Advances
Why Publish With Us?
21DAYS average time to 1st decision
OVER 4 MILLION views in the last year
INCLUSIVE scope
Learn More
AIP Publishing

Journal of Applied Physics | ARTICLE | pubs.aip.org/aip/jap

An electro-thermal finite element method (FEM) model for local hotspot kinetics in $Cu(In, Ga)Se_2$ thin-film solar modules

Cite as: J. Appl. Phys. **136**, 115102 (2024); doi: 10.1063/5.0222051
Submitted: 5 June 2024 · Accepted: 1 September 2024 ·
Published Online: 17 September 2024

Suheir Nofal,[a] Timon S. Vaas,[a] Uwe Rau,[a] and Bart E. Pieters[b]

AFFILIATIONS

Institute of Energy Materials and Devices: Photovoltaics (IMD-3), Forschungszentrum Jülich, 52425 Jülich, Germany

[a]**Also at:** Jülich Aachen Research Alliance (JARA-Energy) and Faculty of Electrical Engineering and Information Technology, RWTH Aachen University, Schinkelstr. 2, 52062 Aachen, Germany.
[b]**Author to whom correspondence should be addressed:** b.pieters@fz-juelich.de

ABSTRACT

Partial shading can significantly impair the efficiency of thin-film solar cells. When exposed to partial shading, cells within the array tend to become reverse biased, leading to thermal runaway events and the emergence of hotspots. In $Cu(In, Ga)Se_2$ (CIGS) solar cells such hotspots are also associated with so-called worm-like defects. Both theoretical and experimental studies have shown that in CIGS, a positive-feedback loop leads to instability and thermal runaway events. However, we observe an inconsistency between published simulation results and recently published experimental work. In a recent experimental study, it was shown that under certain conditions, a hotspot develops within $1\,ms$, showing signs of melting of the CIGS in an area with a $5\,\mu m$ radius. However, in published simulation results, the time for such high temperatures to develop is in the order of seconds, a discrepancy of three orders of magnitude. In this work, we argue that this discrepancy is explained by the size of the seed defect, demonstrating that the origin of these experimentally observed, fast-developing hotspots is likely microscopic defects. To this end, we developed an electro-thermal finite element model, with very high temporal and spatial resolution. We demonstrate that, assuming a seed defect with a $10\,nm$ radius, we can reproduce the experimental results with respect to the size of the defect and the time it took to develop.

29 June 2026 17:12:38

© 2024 Author(s). All article content, except where otherwise noted, is licensed under a Creative Commons Attribution (CC BY) license (https://creativecommons.org/licenses/by/4.0/). https://doi.org/10.1063/5.0222051

I. INTRODUCTION

Partial shading of thin-film solar modules is known to cause reverse bias conditions for one or more cells in a module, leading to the development of hotspots and permanent local shunt-like defects.[1–10] If the reverse bias exceeds the breakdown voltage in a cell, the cell is driven into junction breakdown. As the breakdown voltage can locally be lower than in the surroundings, such a breakdown may occur very locally. Alternatively, there may be pre-existing local defects in the solar cell, leading to a very local dissipation of power. A local power dissipation in the solar cell leads to a rapid increase in temperature and is known to cause permanent damage to a solar cell, reducing its performance.

A large body of literature exists describing the effects of extended reverse bias stress leading to "worm-like" defects in $Cu(In, Ga)Se_2$ solar modules.[1–5] Westin *et al.* was one of the first to report these worm-like defects experimentally, using IR thermography.[1] Phase segregation was observed in the worm-like defects, where defects near the back contact contained Cu-rich compounds.[1] Bakker *et al.* reported that the defected areas changed into a porous material while copper, indium, and gallium migrate toward the back contact.[5]

Most literature on reverse bias damage uses somewhat extended stress conditions (lasting over seconds or more) to investigate reverse bias damage and worm-like defects. However, recently several studies have been presented where short pulses were used. Wendlandt and Podlowski has shown that shunt-like defects were formed within a 10 ms light flash while the modules are partially shaded.[7] Furthermore, Vaas *et al.* have shown that with a 10 ms reverse voltage pulse, defects can be created.[11] In the latter experiments, it was shown that a defect with a size of $10\,\mu m$ was created

© Author(s) 2024

in less than 1 *ms*, where there was no sign of a defect before the reverse bias pulse.[11] As the defects reported in the studies by Vaas *et al.* are very small, we do not refer to these defects as worm-like. However, Vaas *et al.* noted that many defects are elongated, which may be an indication that these small defects can propagate to form worm-like defects.[11] Similarly, Johnston *et al.* demonstrated that such small local hotspots may act as the seeds for worm-like defects.[2,3]

Karpov presented a theory for thermal runaway effects in semiconductor devices.[12] This work developed a theory of transverse electron transport coupled with heat transfer in semiconductor thin films. It is shown that the combination of Joule heating with a thermally activated conductivity leads to a positive feedback and results in instability (thermal runaway).[12] Experimentally, such a positive feedback has been observed recently in CIGS solar cells under reverse bias.[10,13–15]

Based on Karpov's theory,[12] Nardone *et al.* used a coupled electro-thermal finite element model (FEM) to demonstrate that a small shunt-like defect can lead to such a positive feedback loop, thereby causing thermal runaway.[8] In a related paper, with the same coupled FEM model, it was reported that for a CIGS representative device structure, a pre-existing defect with a radius of $2\,\mu$m, resulted in a thermal runaway to $T > 1000$ K occurs within a few seconds.[16] However, as discussed before, recent experiments show thermal runaway effects emerging within 1 ms.[11] Thus, there is a discrepancy of three orders of magnitude in the modeled and observed rate at which a hotspot develops.

In this paper, we introduce an electro-thermal FEM model, similar to the model presented in Refs. 8 and 16, to investigate the development of thermal runaway effects in CIGS solar cells. We theorize that a small pre-existing defect will develop into a hotspot faster than a large defect, as the volume within which the power is dissipated is reduced, thus, leading to a faster heating. For this reason, we use a highly resolved model (both spatially and temporally) and include an initial defect with a 10 nm radius (i.e., a factor 200 smaller than in Ref. 16). The results are compared with experimental data from the experiments presented in Ref. 11. In addition, we study the impact of various material properties within the development of a thermal runaway.

In Sec. II, we briefly discuss the pulsed breakdown experiments. Section III introduced the used electrical and thermal models and their coupling. The main results are presented in Sec. IV. Our full theory behind the thermal runaway effect are described in Sec. V, followed by a summary of the main conclusion in Sec. VI.

II. EXPERIMENTS

The experimental results we use to compare our model with are presented in Ref. 11. These pulsed reverse breakdown experiments were conducted to investigate the time scale of defect creation under reverse bias in CIGS. The used samples consist of two monolithically series-connected cells, with a (glass/Mo/CIGS/CdS/AZO/EVA) layer stack cut from industrial semi-fabricated CIGS modules produced using co-evaporation.[17] The exact thicknesses of all deposited layers can be found in Table I.

The samples are stressed with short (i.e., $t = 10$ ms) reverse voltage pulses. Both the electrical and thermal responses are measured using an oscilloscope and thermal camera, respectively. An in-depth discussion of the experiments and the results are beyond the scope of this paper. Here, we suffice with some of the key findings.

In this paper, we will focus on a single measurement from the experiments in Ref. 11. The electrical response (both voltage and current as a function of time) for this particular measurement is depicted in Fig. 1. In this measurement, a 10 ms pulse of 13.40 V

TABLE I. The used CIGS device properties. The EVA properties are taken from Ref. 21. All remaining properties are from Ref. 22.

Layer name	Thickness d (m)	Thermal conductivity k (W m^{-1} K^{-1})	Specific heat capacity c_p (J kg^{-1} K^{-1})	Density ρ (kg m^{-3})
EVA[21]	0.30×10^{-3}	0.34	1 400	950
AZO	1.05×10^{-6}	23.0	494	5 670
CIGS	2.05×10^{-6}	3.7	300	5 770
Mo	1.00×10^{-6}	138.0	250.7	10 280
Glass	3.00×10^{-3}	1.42	1 154	2 380

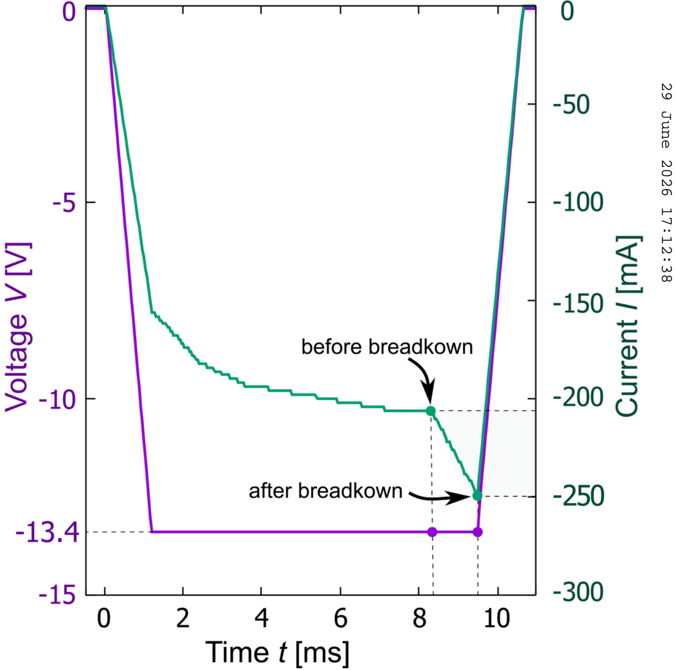

FIG. 1. The electrical response of the sample under investigation, including both the applied voltage (in purple) and the resulting current (in green). The sample, consisting of two series-connected cells, was stressed using a voltage pulse of 13.4 V for 10 ms. A current increase from 210 to 250 mA occurred at $t = 8.25$ ms after the pulse was applied and lasted for almost 1 ms. This current surge indicates a breakdown in one of the cells (while the other cell in the series connection remains unaffected and operates normally), leading to permanent damage in the affected cell as shown in Fig. 2.

29 June 2026 17:12:38

© Author(s) 2024

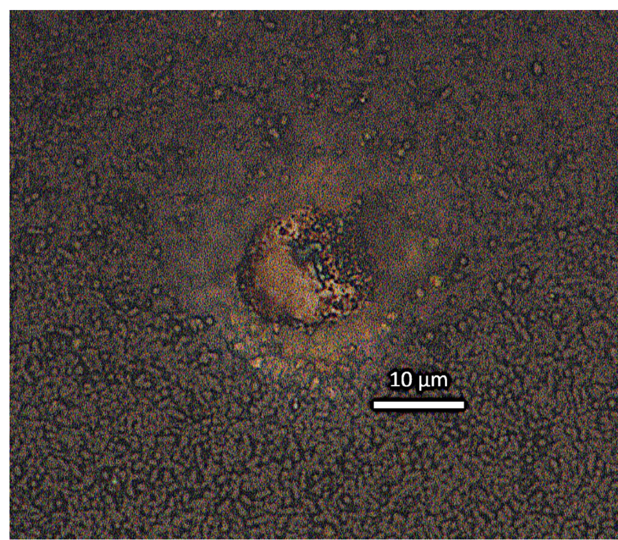

FIG. 2. Microscopic image of a defect with a radius of $5\,\mu$m in a CIGS thin-film solar cell. The image was acquired using an optical microscope after the removal of encapsulation.

reverse voltage was applied to the two series-connected cells. Initially, there was no prior-defect visible in thermography for either cell. During the last 1 *ms* of the pulse, there was a sudden current surge, after which a hotspot became visible in thermography in one of the cells. It is important to note that such a current surge is only, and consistently, observed when a hotspot develops in one cell while the other cell in the series connection remains unaffected and operates normally. In Fig. 2, the defect found in the affected cell after the pulse and removal of encapsulation. The center defect has a radius of about $5\,\mu$m. The observed change in the material indicates the materiel was locally molten, indicating temperatures around the melting temperature of CIGS (i.e., ranging from 990 to 1070 °C[18]). We infer from this experiment that a thermal runaway developed during only the last 1 ms. During this time, the defect developed from something microscopic (invisible in thermography) to a defect of $5\,\mu$m radius.

III. SIMULATION

In the following, we detail our simulation model for reverse bias hotspots in CIGS solar cells. We start with a short discussion on the seed-defect assumption in Sec. III A, which plays a central role in our simulation model. After that, we will discuss the coupled electro-thermal model as it is implemented using freefem++.[19] We discuss the thermal model in Sec. III B, the electrical model in Sec. III C, and the coupling between the electrical and thermal models in Sec. III D.

A. The "seed-defect" assumption

Before we dive into the technical details of our simulation model, it is imperative to underscore the role of pre-existing defects, i.e., seed defects, in our model for the formation of worm-like defects in CIGS solar cells. We are not alone in the assumption a pre-existing defect may grow and evolve into a worm-like defect, for example, Johnston *et al.* and Nardone *et al.*, both assume a pre-existing defect. The works of Westin *et al.* and Bakker *et al.* indicate that once temperatures reach a threshold that permits spinodal decomposition, the CIGS material tends to segregate, forming at least one conductive phase. This formation of a conductive phase can escalate localized power dissipation, creating a positive feedback loop that may not only foster the growth but potentially also the propagation of a defect. It should be noted, however, that there is no proof such a pre-existing defect is always present. In fact, we recently demonstrated a positive feedback in CIGS solar cells under reverse bias using hotspot lock-in thermography (HS-LIT).[14,15] Using HS-LIT, it is possible to observe and quantify a positive loop-gain without causing permanent damage and without any indication of a prior, shunt-like defect. However, even if no pre-existing defect is present, the observed positive feedback may locally heat the cell to the threshold of spinodal decomposition, and latest at this point a shunt-like defect is present, which, from that point onward, may be considered the seed-defect. Another critical point to address is that experiments on reverse bias in CIGS, both in this paper and in other studies, consistently report the presence of shunt-like defects that form hotspots and may propagate through the device. These defects, identified as hotspots, clearly indicate significantly higher conductivity compared to the surrounding reverse-biased diode. Consequently, such conductive shunts reduce the local voltage across the diode near the defect, further diminishing the current through the diode in the vicinity of the hotspot. As a result, the temperature of the device remains unchanged far from the defect, while near the defect, the current bypasses the diode. Therefore, we disregard the thermally activated nature of the diode current in our analysis. This approach also addresses the issue of not being able to provide reliable temperature-dependent diode characteristics up to the critical temperatures of 990–1070 °C observed in the experiments.

29 June 2026 17:12:38

B. Thermal model

The thermal model entails the complete layer stack consisting of glass/Mo/CIGS/AZO/EVA. The initial electrical defect is small both in lateral and vertical dimensions. Thus, we require a full 3D model for the thermal system. Furthermore, as we are interested in the dynamics of a thermal runaway process, the thermal model needs to be a transient model. The 3D transient heat equation is formulated as

$$k\nabla^2 T + P(t) = \rho c_p \frac{\partial T}{\partial t}, \tag{1}$$

where k is the thermal conductivity, T is the temperature, P is the locally dissipated electrical power, t is time, ρ is the density of the medium, and c_p is the specific heat capacity.

We consider solutions of Eq. (1) in a 3D cylindrical domain representing the solar cell layer stack, as illustrated in Fig. 3. The defect is located laterally in the center of the cylindrical domain. Vertically the defect is located in the electrically relevant part,

© Author(s) 2024

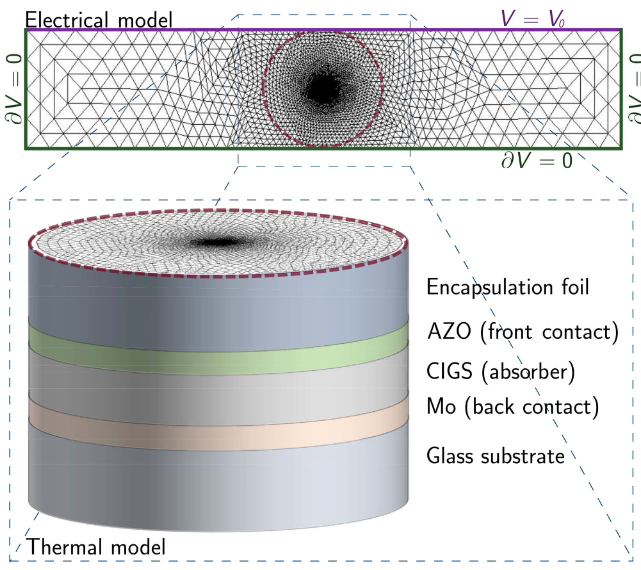

FIG. 3. Schematic illustration of the mesh for both electrical and thermal models. The electrical model is rectangular with dimensions of $0.4 \times 2\,\text{cm}^2$, while the thermal model is cylindrical with a diameter equals the width of the cell (i.e., 0.40 cm), and a depth equals the thickness of all layers in the stack as in Table I.

i.e., the CIGS and AZO layers. We use a variable mesh to create a highly resolved mesh around the defect, achieving maximal triangulation of the nodes.

The convective heat loss at the front and back surface of the stack is taken into account with a Neumann boundary condition according to

$$\frac{\partial T}{\partial \mathbf{n}} = -b(T - T_{\text{amb}}), \tag{2}$$

where $\mathbf{n}$ is the exterior normal of the boundary, b is a convective heat loss term, and T_{amb} is the ambient temperature.

For the vertical cylindrical boundary, we apply a Dirichlet boundary condition with $T = T_{\text{amb}}$. However, we choose the diameter of the cylindrical domain such that that $\frac{\partial T}{\partial \mathbf{n}} \approx 0$ for all simulations in this work (i.e., the lateral simulation domain is chosen large enough to represent a semi-infinite xy-plane). For the simulations in this work, we found a radius of 0.2 cm to be sufficient to meet this requirement.

We exclude radiative heat transfer, characterized by its T^4 dependence, from our model due to the highly localized nature of high-temperature regions within the layer stack, particularly around shunt-like defects. These localized hotspots are effectively insulated from direct radiative cooling to the ambient environment by the surrounding device layers and encapsulating materials. Moreover, convective cooling, which is included in our model, primarily occurs at the encapsulation surface, at a significant distance from these internal high-temperature zones. Given the relatively short timescales of our simulations, the increase in surface temperature of the device is minimal, further reducing the potential impact of radiative heat transfer.

For the thermal properties of various materials, we used the parameters listed in Table I. These parameters were found in the literature (appropriate references are indicated in Table I). Moreover, we set the convective heat loss term to $b = 12\,\text{W m}^{-2}\,\text{K}^{-1}$, and the ambient temperature to $T_{\text{amb}} = 22\,^\circ\text{C}$.

C. Electrical model

We expect the electrical response to be much faster than the thermal response. Thus, we consider a steady-state solution for the electrical model. The electrically relevant part of the system consists of several thin films (Mo/CIGS/AZO). As the Mo electrode is much more conductive than the AZO electrode ($R_b \gg R_f$), we consider the Mo as a perfect conductor, while the resistance in the AZO electrode is represented as the sum of both components, $R_{\text{sheet}} = R_f + R_b$. Consequently, we may limit the electrical model to describe the potential in the AZO. As the resulting electrical model consists only of a single thin film, we may solve this problem in a 2D domain. Within a 2D electrode, the steady-state potential may be described with Poisson's equation,[23]

$$\nabla^2 V(x, y) = R_{\text{sheet}} J(x, y), \tag{3}$$

where V is the local voltage, R_{sheet} is the electrode sheet resistance (per square), and J is the current density through the solar cell (i.e., out of the electrode).

If we linearize the current density through the solar cell, we can rewrite Eq. (3) as

$$\nabla^2 V(x, y) = R_{\text{sheet}} \frac{V(x, y)}{R(x, y)}, \tag{4}$$

where R is the electrical resistivity of the solar cell. For $R(x, y)$, we assume two phases in the electrical system. A defected phase with $R = R_{\text{def}}$ and a non-defective phase $R = R_{\text{non-def}}$.

As the CIGS solar cell consists of a rectangular cell-stripe, the boundary value problem consists of a rectangular domain with one Dirichlet boundary ($V = V_0$) along one edge, and a Neumann boundary ($\partial V = 0$), along the remaining three edges,[23] as illustrated in Fig. 3.

In this work, we consider a rectangular cell with a width of 0.40 *cm* and a length of only 2.0 cm. Note that the lateral dimensions for the electrical model exceed those of the domain we consider for the thermal simulations. However, the electrical dissipation is generally dominated by the defect, and thus the electrical power dissipation is still mostly confined within the domain considered in the thermal simulations. The initial defect radius is varied in this work. However, the smallest initial defect size we consider is 10 nm.

We parameterize the model according to the experiment discussed in Sec. II as shown in Table II. The voltage over the two series-connected cells is $-13.4\,\text{V}$, while the current is around $-210\,\text{mA}$ before the breakdown and dropped to a higher negative current of $-250\,\text{mA}$ after the hotspot creation. With a cell area of $8.4 \times 0.40\,\text{cm}^2$, we can estimate the current density over the cell area before the breakdown as $62.5 \times 10^{-3}\,\text{mA cm}^{-2}$.

29 June 2026 17:12:38

© Author(s) 2024

TABLE II. The electrical properties of CIGS devices used for this work.

Parameter	Value
Voltage over two cells (V)	-13.4 V
Current before breakdown (I_{bb})	-210 mA
Current after breakdown (I_{ab})	-250 mA
Current density (J)	62.5×10^{-3} mA cm^{-2}
CIGS resistance ($R_{non-def}$)	$107\,\Omega\,cm^2$
Sheet resistance (R_{sheet})	$24\,\Omega$

The non-defected, active part of CIGS would then have an average resistance of $R_{non-def} = (13.4/2)/(62.5) = 1.07 \times 10^2\,\Omega\,cm^2$.

As the experimental procedure involves a sample with two series-connected cells, the voltage is being divided between them. Before breakdown, it is anticipated that the voltage is evenly distributed, with each cell receiving approximately half of the applied voltage, as previously described. However, only one cell broke down, hence during breakdown, the exact voltage distribution becomes uncertain. Consequently, we opt for a current-driven approach in the simulation to ensure that the current matches the breakdown current, as we know that the two adjacent cells will have the same current value. We assume the defected area to be very conductive. The shunt resistance of the defected phase R_{def} is one of the parameters under investigation. We vary the value of R_{def} over a wide range. The minimum value is based on the electrical resistivity of a pure copper crystal (i.e., $1.678 \times 10^{-8}\,\Omega\,cm$ at $20\,^{\circ}C$),[24] and the maximum value is the non-defected resistivity $R_{non-def}$. For the AZO electrode sheet resistance, we rely on data provided by the CIGS module manufacturer, $R_{sheet} = (R_f + R_b) = 24\,\Omega$.

D. Coupling

To study Joule-heating in an electrical system, we need to couple the electrical and thermal models. To this end, we need to extract the electrical power dissipation from the electrical system and map this dissipation to the corresponding volumes in the thermal system. This coupling is illustrated in Fig. 4.

From the electrical model in Eq. (4), we compute the power density in the AZO electrode as

$$P_{AZO}(x, y) = \frac{|\nabla V|^2}{R_{sheet}}, \quad (5)$$

where $|\nabla V|$ is the electric field (F) within the electrode. Likewise, the power dissipation in the CIGS solar cell is computed as

$$P_{CIGS}(x, y) = V^2 G(x, y), \quad (6)$$

where $G(x, y)$ is the electrical conductivity.

The power dissipation from Eq. (5) is mapped to the AZO layer. Note that the power density from Eq. (5) is in W m^{-2}. By distributing the power uniformly over the AZO layer thickness, we compute a power density in W m^{-3} to inject in the electrical system. In a similar way, we map the electrical power density from Eq. (6) to the CIGS layer. However, most of the power dissipation in the solar cell is limited to the depletion width in the solar cell. For simplicity, we map the dissipated power density from Eq. (6) uniformly to the top third of the total CIGS layer thickness.

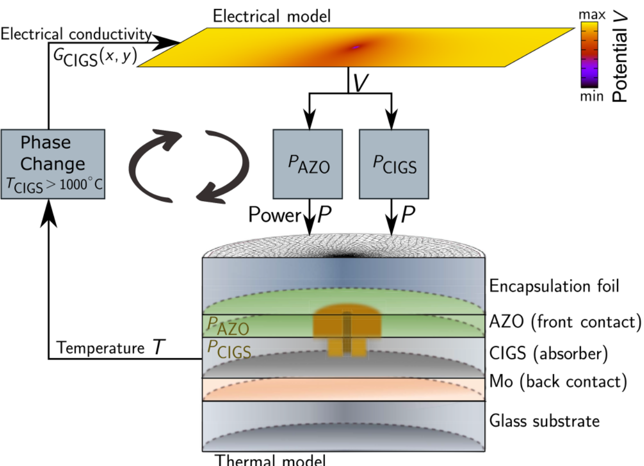

FIG. 4. Schematic illustration of the coupled electro-thermal model. The two models are linked via electrical power from the electrical model and temperature distribution from the thermal model at each time iteration. The electrical power is calculated and mapped in both AZO and CIGS layers. The temperature of each FEM triangle in the middle of the CIGS layer is evaluated, if it exceeds the melting temperature of CIGS, the resistance of the corresponding area in the electrical mesh is shifted from non-defected to defected values.

As illustrated in Fig. 4, there is also a coupling back from the thermal model to the electrical model. This coupling is via the defective and non-defective phases in the electrical model. We assume that beyond a critical temperature, T_{crit}, the CIGS undergoes permanent structural changes (i.e., the CIGS becomes porous with copper, indium, and gallium migrating toward the back contact[5]).

The melting point of CIGS is between 990 and $1070\,^{\circ}C$.[18] Given this relatively narrow range, we choose $T_{crit} = 1000\,^{\circ}C$ as the threshold value for our model. Considering the narrow melting point range, we expect any variations due to threshold adjustments to be minimal.

If the temperature within the CIGS exceeds this temperature, we change the phase from non-defected to defected. In other words, the temperature of each triangular element within the finite element mesh of the CIGS layer is evaluated in the thermal model. If it exceeds the $1000\,^{\circ}C$, the resistance of that corresponding region is switched from non-defected to defected resistance in the electrical mesh. Note, however, that this change is permanent, i.e., the defected phase never changes back to non-defected even if the FEM triangle cools down in the following iterations. This phase change allows the defect to grow.

The solution of the coupled electro-thermal model starts by solving the electrical model in Eq. (4) and mapping the dissipated power densities in both AZO and CIGS layers from Eqs. (5) and (6), respectively, to the thermal system as shown in Fig. 4. Subsequently, we simulate the transient thermal model until we find the temperature within the CIGS exceeds the critical temperature. If this is the case, the electrical model of Eq. (4) is updated and the new power dissipation from Eqs. (5) and (6) are mapped again to the appropriate volumes in the simulation domain.

29 June 2026 17:12:38

© Author(s) 2024

For time discretization, we apply a semi-adaptive time step where the time step is linked to the defect area. As, in general, the maximum dissipated power density decreases with increasing defect radius, the time step can increase for larger defects without much loss of accuracy.

E. Discussion

As a final note, we would like to shortly discuss the difference between current- and voltage-driven experiments. In this work, we have opted to simulate a current-driven experiment, i.e., the current is kept constant. In current-driven experiments, the creation of defects will reduce the voltage over the device and subsequently quench the power dissipation at hotspots. In contrast, in voltage-driven experiments, the current will increase, potentially accelerating the growth and evolution of hotspots due to increased power dissipation.

We would like to argue here that voltage-driven experiments do not accurately reflect real-world field conditions for reverse bias damage. In practical scenarios, reverse bias damage is predominantly current-driven. Commercial CIGS modules typically operate with maximum power point voltages ranging from 60 to 85 V. This relatively high voltage allows the maximum power point current (I_{mpp}) to pass through shaded cells, largely independent of their specific breakdown voltages, which are typically an order of magnitude lower. Consequently, in real-world applications, reverse bias damage occurs under near-constant current conditions, rather than constant voltage.

IV. RESULTS

A. Baseline

We first present a baseline for our simulation results. For this baseline, we set the defect resistance to $R_{\mathrm{def}} = 3.14 \times 10^{-7}\,\Omega\,\mathrm{cm}^2$. In Fig. 5 we show the results for the baseline simulation after $5\,\mu$s. In Fig. 5(a) the temperature is depicted. In the center of this graph, the temperature exceeds the critical temperature of $1000\,^{\circ}$C. Accordingly in Fig. 5(b) the phase map exhibits a defect with an approximate radius of $2.5\,\mu$m (compared to an initial radius of 10 nm). The corresponding power densities in the AZO and CIGS layers are shown in Figs. 5(c) and 5(d), respectively. From Fig. 5(c) we observe that the dissipated power density in the AZO increases toward the defect and suddenly drops to $0\,\mathrm{W\,m^{-3}}$ within the defect. This is expected as current crowding at the edge of the defect leads to higher dissipation toward the defect. In Fig. 5(d), we see the power dissipation is within the whole area of the defect reaching its maximum at the circumference of the defect as the power is generated in the Cu(In, Ga)Se_2 layer itself.

Figure 6 shows the results when the defect has reached a radius of $6.2\,\mu$m after 0.55 ms. In Fig. 6(a), the temperature is shown. The temperature of a larger area exceeds the critical temperature of $1000\,^{\circ}$C. Consequently, the phase map in Fig. 6(b) shows a larger defect. The defect is not exactly circular anymore, but the effective radius is $6.2\,\mu$m, where we determined the effective radius from the defect area (e.g., $A_{\mathrm{def}} = \pi r_{\mathrm{eff}}^2$). Figures 6(c) and 6(d) depict power densities in the AZO and CIGS layers, respectively. Comparing the results to Figs. 5(c) and 5(d), respectively, we observe the electrical power density decreased considerably for the larger defect radius. This is a direct consequence of the increased size as with a larger defect we expect less current crowding at the edge of the defect. Furthermore, in Fig. 6(c), we observe higher power density along the contour of the defected area. These areas with higher power density correspond to the areas with higher power density at the circumference of the defect in Fig. 6(d). Comparing the locations of areas with higher power density in Figs. 6(c) and 6(d) with the phase plot in Fig. 6(b), we can see that the non-smooth circumference is caused by the ragged contour of the defect. However, this ragged nature of the contour is related to the simulation mesh, i.e., at this point in the

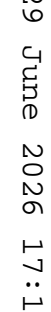
29 June 2026 17:12:38

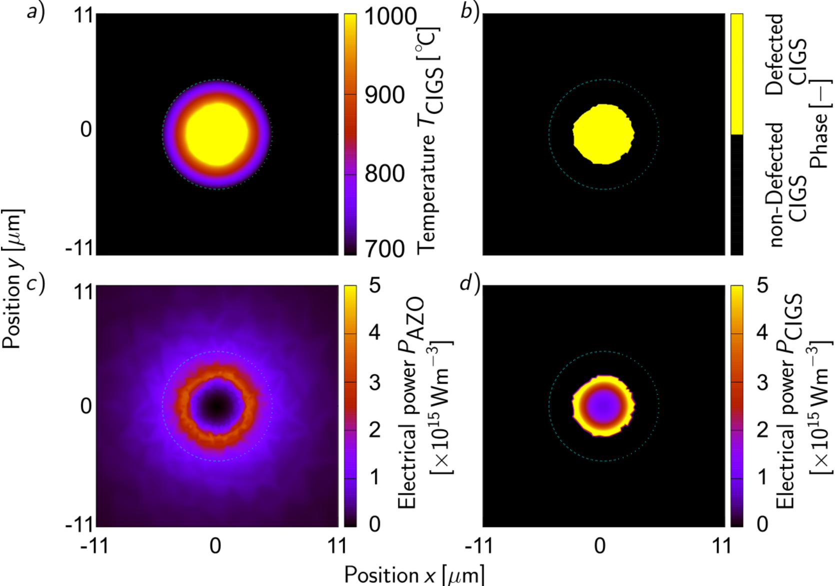

FIG. 5. (a) Temperature distribution profile in the middle of CIGS layer, (b) phase plot, (c) AZO power profile, and (d) CIGS power distribution. The current is injected from the top long edge of the cell. Defect resistance is $3.14 \times 10^{-7}\,\Omega\,\mathrm{cm}^2$. Cyan circle indicates a radius of $5\,\mu$m. The defect has reached a radius of around $2.5\,\mu$m after $5\,\mu$s.

© Author(s) 2024

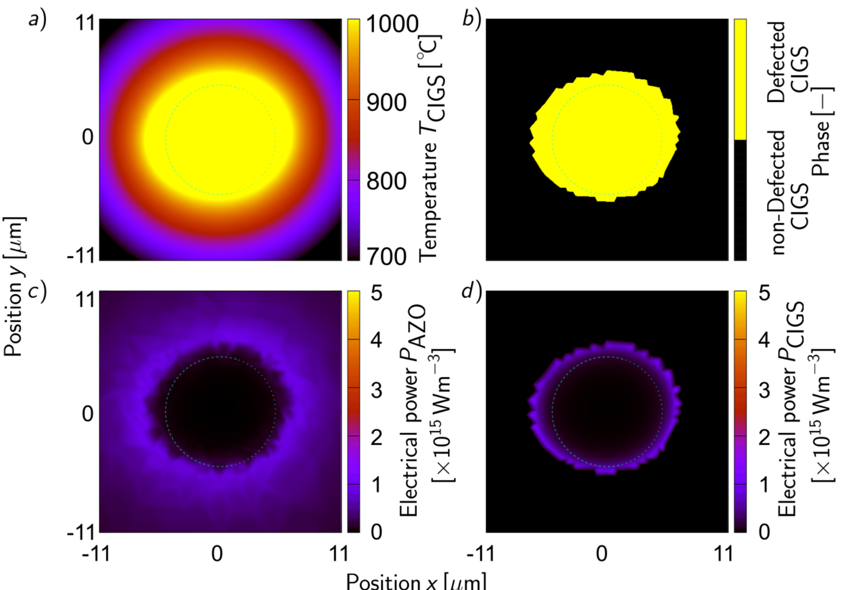

FIG. 6. (a) Temperature distribution profile in the middle of CIGS layer, (b) phase change plot, (c) AZO power profile, and (d) CIGS power distribution. The current is injected from the top long edge of the cell. Defect resistance is $3.14 \times 10^{-7}\,\Omega\,\mathrm{cm}^2$. Cyan circle indicates a radius of 5μm. The defect has reached a radius of around 6.2$\,\mu$m after 0.55 ms.

simulation the resolution of the mesh is too low to produce a sufficiently smooth contour of the defect.

B. Time evolution and parameter variation

In Fig. 7, we show the effective radius of the defect size as a function of time. The effective radius is defined as the radius for which a circle has the same area as the defect area in the simulations (in the simulations the defect is not always perfectly circular). For these simulations, we varied the defect resistance between the values 3.14×10^{-5}, 3.14×10^{-7} and $3.14 \times 10^{-9}\,\Omega\,\mathrm{cm}^2$. The results for the baseline simulation, corresponding to the results in Figs. 5 and 6, are shown in green.

Starting with the baseline simulation in Fig. 7, which has a defect resistivity of $3.14 \times 10^{-7}\,\Omega\,\mathrm{cm}^2$, the defect initially remains stable with no growth. This is followed by a rapid growth phase where the defect radius increases by more than an order of magnitude. Subsequently, a more steady and gradual growth is observed, with the defect reaching a radius of 6.2$\,\mu$m after 0.55 ms. Following this point, the defect did not grow more up until the end of the simulated time frame of 1 ms. We would like to stress that this does not imply stability; the defect's growth clearly slows down as more time is required to heat a larger volume. However, hot spots and worm-like defects evolve over the time frame of many seconds, which is beyond the scope of this paper.

29 June 2026 17:12:38

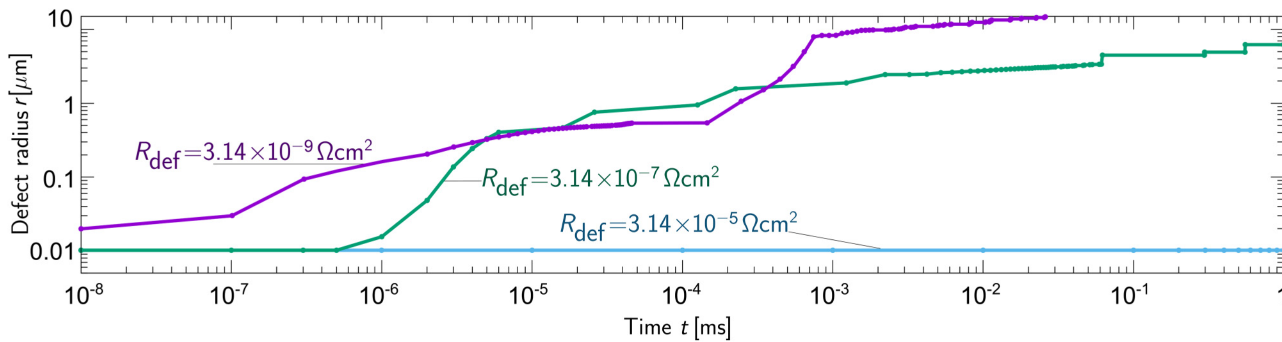

FIG. 7. Growth of a defect illustrated by the change of the effective radius r as a function of time t. The shunt resistance of defected CIGS (R_{def}) is taken as the parameter under investigation. The defect resistivity (i.e., $3.14 \times 10^{-7}\,\Omega\,\mathrm{cm}^2$) after a short delay show a phase of rapid growth toward a radius of approximately 1$\,\mu$m followed by a phase of relatively slower growth toward several micrometers. A lower resistivity has a faster growth behavior at the initial stages and exhibits a phase of rapid growth later in time. Notably the timing when the explosive growth takes place is dependent on the assumed R_{def} and the dissipated power in both AZO and CIGS layers. A higher resistivity, on the other hand, leads to no growth in the defect. The green curve corresponds to the baseline shown in Figs. 5 and 6.

© Author(s) 2024

In comparison, the defect growth with a lower resistivity (defect resistivity of $3.14 \times 10^{-9}\,\Omega\,\mathrm{cm}^2$) exhibits a much faster growth from a very early stage in time followed by a steep increase in the growth where the defect has reached a radius $\gg 15\,\mu$m in less than the simulation period of 1 ms. On the other hand, a higher defect resistivity of $3.14 \times 10^{-5}\,\Omega\,\mathrm{cm}^2$ results in no defect growth by the end of the 1 ms.

In the next step, we further investigate the impact of the resistivity of the defected area in terms of the amount of electrical power dissipated in the defect. We only consider the electrical model in order to evaluate the electrical power dissipation. Figure 8 shows the power dissipation integrated over an area around the defect with a $20\,\mu$m radius. This specific area was selected in order to compare various cases more effectively while varying other parameters including the defect size and its resistivity. Thus, this figure describes how much power is deposited at the defect area, e.g., the power coupling of the defect to the electrical power source. In Fig. 8, we distinguish between the integrated power in the AZO and CIGS layers, and the total (sum) of both contributions. Furthermore, we vary the defect resistance (i.e., 3.14×10^{-5}, 3.14×10^{-7} (baseline), and $3.14 \times 10^{-9}\,\Omega\,\mathrm{cm}^2$).

As depicted in Fig. 8(a), for a defect resistivity of $3.14 \times 10^{-5}\,\Omega\,\mathrm{cm}^2$, the power dissipation in the CIGS layer shows a distinct peak at larger defect radii ($10\,\mu$m), while the maximum power dissipation in the AZO layer forms a much smaller peak. In Fig. 8(b), with the defect resistivity decreased to $3.14 \times 10^{-7}\,\Omega\,\mathrm{cm}^2$, the height and position of the peak power dissipation in the CIGS shift as a function of defect radius. Lower defect resistivity results in a reduced peak power magnitude and a shift toward smaller defect sizes. Conversely, power dissipation in the AZO layer increases, forming a broad peak over a wide range of defect radii. Notably, when the defect size reaches after approximately $1\,\mu$m, there is a significant drop in power dissipation in the AZO layer, leading to slow or no further growth in defect size, as shown earlier in Fig. 7. Likewise, in Fig. 8(c), for a defect resistivity of $3.14 \times 10^{-9}\,\Omega\,\mathrm{cm}^2$, power dissipation in the CIGS shifts to smaller radii with a decreased magnitude, while the maximum power dissipation in the AZO layer is higher, forming a broader plateau across a wider range of defect radii. It is important to note that in all scenarios, a significant proportion of power is dissipated in the CIGS layer at relatively smaller defect sizes, while at larger defect radii, more power tends to dissipate in the AZO layer.

The observed maxima in the power dissipation in the defect, as seen in Fig. 8, is the result of the power being limited by a low voltage over the defect when the resistance is low. As the resistance increases the power may increase. However, if the resistance increases further, the power may drop as the current through the defect decreases. The dissipated power in the AZO behaves differently as it

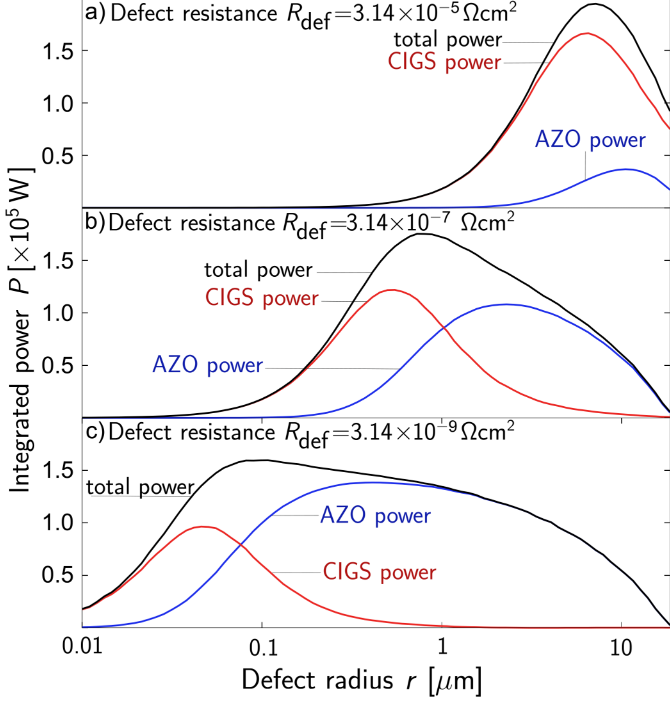

FIG. 8. The dissipated electrical power obtained from the electrical model and integrated separately over the Al:ZnO (AZO) layer and the CIGS layer as a function of the defect radius, over an area around the defect with a $20\,\mu$m radius. We vary the defect resistance to (a) $3.14 \times 10^{-5}\,\Omega\,\mathrm{cm}^2$ (baseline), (b) $3.14 \times 10^{-7}\,\Omega\,\mathrm{cm}^2$ (baseline), and (c) $3.14 \times 10^{-9}\,\Omega\,\mathrm{cm}^2$. At smaller radii most of the power is dissipated in the CIGS, while at larger radii more power is dissipated in the AZO layer. The total power (sum of power in CIGS and AZO) displays a maximum at a distinct defect radius that, in turn, depends on the assumed defect resistance R_{def}.

29 June 2026 17:12:38

© Author(s) 2024

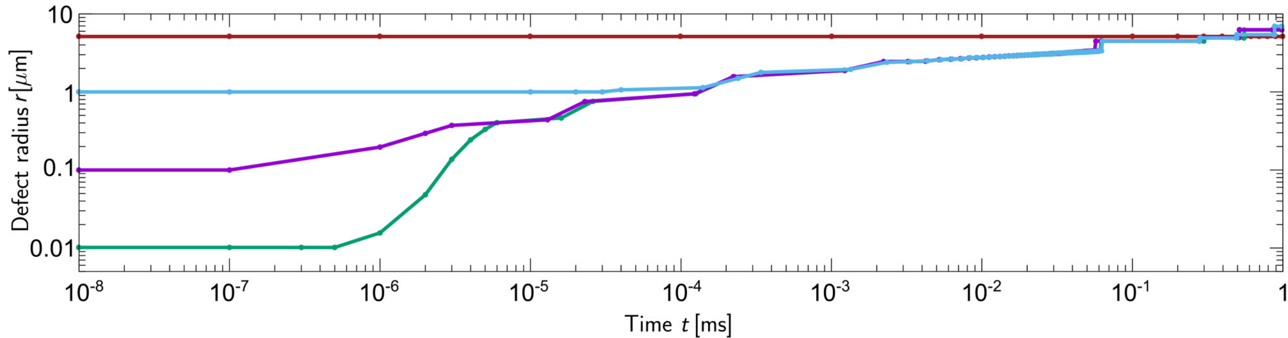

FIG. 9. Growth of a defect as a function of time t due to the change in its initial radius r_0. All simulations the shunt resistance of defected CIGS (R_{def}) as the baseline values of $3.14 \times 10^{-7}\,\Omega\,\text{cm}^2$. The initial defect is varied to radii of 10 nm, 0.1 μm, 1 μm, and 5 μm. No remarkable difference is observed between a radius of 10 nm, 0.1 μm, and 1 μm. After the small defect reaches a radius around 1 μm, a slower growth is observed similar to the behavior in Fig. 7, resulting in a defect size of 6 μm after 1 ms. No change in size is observed for the large defect with a radius of 5 μm. The green curve corresponds to the baseline shown in Figs. 5–7.

only depends on the current through the defect, and hence it is high when the defect resistance is low and drops when the resistance increases.

The results in Fig. 8 are expected to influence the dynamics of hotspot development, as we expect that especially for small and conductive defects the power dissipation is high. As the defect increases in size, the total power dissipation in the defect decreases, and hence the rate at which the hotspot develops will decrease. For a higher defect resistance value there may be a certain defect size for which the power dissipation exhibits a maximum, which may lead to a fast hotspot development for a certain range of defect sizes. Thus, the results in Fig. 8 partly explain the very non-uniform growth rate observed in Fig. 7. Note that the results in Fig. 8 only consider the absolute electrical power deposited, i.e., not the power density.

For our baseline simulation and as shown in Fig. 8(b) with a $3.14 \times 10^{-7}\,\Omega\,\text{cm}^2$, the total power dissipation exhibits its maximum in the region around 1 μm. Nevertheless, we believe that the smaller the defect is the faster it tends to grow. To further investigate this matter we change the size of the initial defect in the simulations while keeping the defect resistance fixed at the baseline value. We specifically vary the initial defect to radii of 0.1 μm, 1 μm, and 5 μm while we limit the simulation time to the 1 ms as the baseline. In Fig. 9, we depict the growth process for all simulations and focus on the early stages. We notice that with 0.1 and 1 μm we obtain the same final radius as the baseline results (about 6 μm after 1 ms). However, with 5 μm we observe no change in defect size through out the simulation and by the end of the 1 ms as the power is not sufficient to heat up the defected area to the threshold temperature of 1000 K.

V. DISCUSSION

As discussed in Sec. III A, we assume a seed defect which gives rise to a positive feedback effect and a thermal runaway. Also in the absence of a shunt-like defect such a positive feedback effect is observed in CIGS solar cells under reverse bias.[14,15] Thus we argue, the initial defect leading to a hotspot and permanent damage, need not be a shunt-like defect. Possibly, early junction breakdown caused by microscopic defects, such as observed in microcrystalline silicon,[25] triggers this positive feedback effect leading to a thermal runaway and the creation of the small initial shunt-like defect.

In light of these considerations, we propose a three-phase process leading to "worms" in CIGS. In the first "nucleation" phase, the thermal activation of the junction breakdown current in CIGS, as experimentally demonstrated in Ref. 10, leads to instability and a thermal runaway starts to develop. The first phase ends when the temperature is high enough for spinodal decomposition to take place, and the CIGS segregates, producing at least one conductive phase.[1,20] At this point, the process becomes irreversible and a shunt-like defect emerges. In the second "growth" phase, the shunt-like defect grows from a small initial defect to a defect with a diameter in the order of micrometers. This phase is covered by this work. In the third and final "wandering" phase, the defect starts to propagate through the solar cell. As this phase can last for a few seconds,[1,20] it falls outside the scope of our present study.

29 June 2026 17:12:38

VI. CONCLUSION

In this work we explain the, experimentally shown, short timescales in which a hotspot may form in CIGS solar cells under reverse bias. To this end, we developed an electro-thermal FEM model with a high spatial and temporal resolution. This way we demonstrated that the experimentally observed time scales for hotspot development are reproduced when assuming a small initial defect size of 10 nm. With such a small initial defect, the experimentally observed final size of the defect (i.e., 5 μm), develops within 1 ms. To achieve these results, with our coupled electro-thermal FEM model, we investigated the unknown material properties including defect resistivity, as well as the initial defect size, while all other parameters in the solar cell are known from the literature. Notably, we observed a significant interplay between the defect size, defect resistivity, and the amount of power deposited at the defect. We demonstrate that there is a maximum in the deposited power which depends on the defect resistivity and radius, where a more conductive defect has its maximum in deposited power at a smaller radius. It is expected that this coupling between defect resistivity and defect size affects the dynamics of the defect evolution, and partly explains the non-uniform growth

© Author(s) 2024

rate we observe in simulations. However, due to the experimental nature of the study, our understanding of the growth process at $t \ll 1$ ms is restricted. Nevertheless, we can still anticipate potential coupling scenarios that result in the experimental defect size at $t = 1$ ms. Finally, we propose a three-phase mechanism for the creation of worms consisting of "nucleation," "growth," and "wandering." In the nucleation phase, junction breakdown (possibly an early breakdown at microscopic electronic defects) trigger a positive feedback loop leading to thermal runaway and spinodal decomposition, creating a small initial shunt-like defect. In the growth phase, this defect grows larger (by the mechanisms described in this work). In the final phase, the defect starts to wander through the solar cell, leading to a worm-like defect.

ACKNOWLEDGMENTS

This work was partially supported by the German Federal Ministry of Education and Research (BMBF: Funding Reference No. 01DH16027) within the framework of the Palestinian-German Science Bridge project, and the OptiCIGSII project (No. FK0324297D) funded by the Federal Ministry of Economics and Technology BMWK.

AUTHOR DECLARATIONS

Conflict of Interest

The authors have no conflicts to disclose.

Author Contributions

Suheir Nofal: Data curation (equal); Formal analysis (equal); Investigation (equal); Methodology (equal); Software (equal); Validation (equal); Writing – original draft (equal); Writing – review & editing (equal). **Timon S. Vaas:** Investigation (equal); Writing – review & editing (equal). **Uwe Rau:** Conceptualization (equal); Project administration (equal); Resources (equal); Writing – review & editing (equal). **Bart E. Pieters:** Conceptualization (equal); Data curation (equal); Formal analysis (equal); Methodology (equal); Software (equal); Supervision (equal); Validation (equal); Visualization (equal); Writing – review & editing (equal).

DATA AVAILABILITY

The data that support the findings of this study are available from the corresponding author upon reasonable request.

REFERENCES

[1]P.-O. Westin, U. Zimmermann, L. Stolt, and M. Edoff, "Reverse bias damage in CIGS modules," in *24th European Photovoltaic Solar Energy Conference and Exhibition* (WIP Wirtschaft und Infrastruktur GmbH & Co Planungs-KG, 2009).
[2]S. Johnston, E. Palmiotti, A. Gerber, H. Guthrey, L. Mansfield, T. J. Silverman, M. Al-Jassim, and A. Rockett, "Identifying reverse-bias breakdown sites in $CuIn_xGa_{1-x}Se_2$," in *2017 IEEE 44th Photovoltaic Specialist Conference (PVSC)* (IEEE, 2017), pp. 1400–1404.
[3]S. Johnston, D. Sulas, E. Palmiotti, A. Gerber, H. Guthrey, J. Liu, L. Mansfield, T. J. Silverman, A. Rockett, and M. Al-Jassim, "Thin-film module reverse-bias breakdown sites identified by thermal imaging," in *2018 IEEE 7th World Conference on Photovoltaic Energy Conversion (WCPEC) (A Joint Conference of 45th IEEE PVSC, 28th PVSEC 34th EU PVSEC)* (IEEE, 2018), pp. 1897–1901.
[4]E. Palmiotti, S. Johnston, A. Gerber, H. Guthrey, A. Rockett, L. Mansfield, T. J. Silverman, and M. Al-Jassim, "Identification and analysis of partial shading breakdown sites in $CuIn_xGa_{1-x}Se_2$ modules," Sol. Energy **161**, 1–5 (2018).
[5]K. Bakker, H. Nilsson Åhman, K. Aantjes, N. Barreau, A. Weeber, and M. Theelen, "Material property changes in defects caused by reverse bias exposure of CIGS solar cells," IEEE J. Photovoltaics **9**, 1868–1872 (2019).
[6]T. J. Silverman, M. G. Deceglie, X. Sun, R. L. Garris, M. A. Alam, C. Deline, and S. Kurtz, "Thermal and electrical effects of partial shade in monolithic thin-film photovoltaic modules," IEEE J. Photovoltaics **5**, 1742–1747 (2015).
[7]S. Wendlandt and L. Podlowski, "Influence of near field shadowing on the performance ratio of thin film modules," in *Proceedings of 35th European Photovoltaic Solar Energy Conference and Exhibition* (WIP Wirtschaft und Infrastruktur GmbH & Co Planungs-KG, 2018), pp. 1230–1235.
[8]M. Nardone, S. Dahal, and J. Waddle, "Shading-induced failure in thin-film photovoltaic modules: Electrothermal simulation with nonuniformities," Sol. Energy **139**, 381–388 (2016).
[9]H. Lv, W. Huang, C. Cheng, Y. Ou, J. Liao, Y. Su, and S. Riffat, "An improved model to predict thermal runaway in concentrator III-V multi-junction solar cells," Int. J. Low-Carbon Technol. **13**, 432–437 (2018).
[10]S. J. Heise, A. Komilov, M. Richter, B. Pieters, A. Gerber, and J. Neerken, "Reverse-bias behaviour of thin-film solar cells: Effects of measurement-induced heating," EPJ Photovoltaics **14**, 17 (2023).
[11]T. S. Vaas, B. E. Pieters, A. Gerber, and U. Rau, "Reverse-bias defect creation in Cu(In, Ga)Se_2 solar cells and impact of encapsulation," Solar **3**, 184–194 (2023).
[12]V. Karpov, "Coupled electron–heat transport in nonuniform thin film semiconductor structures," Phys. Rev. B **86**, 165317 (2012).
[13]T. S. Vaas, B. E. Pieters, A. Gerber, and U. Rau, "Thermal stimulation of reverse breakdown in CIGS solar cells," IEEE J. Photovoltaics **PP**, 1–6 (2023).
[14]S. Nofal and B. Pieters, "A novel non-destructive characterization method to investigate hot-spot formation in CIGS solar cells using lock-in thermography," in *IEEE 48th Photovoltaic Specialists Conference (PVSC)* (IEEE, 2021), pp. 1328–1330.
[15]S. Nofal, B. E. Pieters, M. Hülsbeck, C. Zahren, A. Gerber, and U. Rau, "A direct measure of positive feedback loop-gain due to reverse bias damage in thin-film solar cells using lock-in thermography," EPJ Photovoltaics **14**, 6 (2023).
[16]H. Guthrey, M. Nardone, S. Johnston, J. Liu, A. Norman, J. Moseley, and M. Al-Jassim, "Characterization and modeling of reverse-bias breakdown in Cu(In, Ga)Se_2 photovoltaic devices," Prog. Photovoltaics: Res. Appl. **27**, 812–823 (2019).
[17]B. Dimmler and R. Wächter, "Manufacturing and application of CIS solar modules," Thin Solid Films **515**, 5973–5978 (2007).
[18]T. Tinoco, C. Rincón, M. Quintero, and G. S. Pérez, "Phase diagram and optical energy gaps for $CuIn_yGa_{1-y}Se_2$ alloys," Phys. Status Solidi A **124**, 427–434 (1991).
[19]F. Hecht, "New development in freefem++," J. Numer. Math. **20**, 251–265 (2012).
[20]K. Bakker, H. N. Åhman, T. Burgers, N. Barreau, A. Weeber, and M. Theelen, "Propagation mechanism of reverse bias induced defects in Cu(In, Ga)Se_2 solar cells," Sol. Energy Mater. Sol. Cells **205**, 110249 (2020).
[21]J. Speight and N. Lange, *Lange's Handbook of Chemistry*, 16th ed. (McGraw-Hill, New York, 1992).
[22]W. Haynes, *CRC Handbook of Chemistry and Physics* (CRC Press, 2014).
[23]B. E. Pieters and U. Rau, "A new 2D model for the electrical potential in a cell stripe in thin-film solar modules including local defects," Prog. Photovoltaics: Res. Appl. **23**, 331–339 (2015).
[24]R. A. Matula, "Electrical resistivity of copper, gold, palladium, and silver," J. Phys. Chem. Ref. Data **8**, 1147–1298 (1979).
[25]O. Breitenstein, J. Bauer, K. Bothe, W. Kwapil, D. Lausch, U. Rau, J. Schmidt, M. Schneemann, M. C. Schubert, J.-M. Wagner, and W. Warta, "Understanding junction breakdown in multicrystalline solar cells," J. Appl. Phys. **109**, 071101 (2011).

29 June 2026 17:12:38

© Author(s) 2024